Journal of Wind Engineering & Industrial Aerodynamics 240 (2023) 105447

Contents lists available at ScienceDirect

Journal of Wind Engineering & Industrial Aerodynamics

journal homepage: www.elsevier.com/locate/jweia

Wind and structural response monitoring of a lighting pole for the study of downburst effects on structures

Mekdes T. Mengistu *, Andrea Orlando, Maria Pia Repetto

University of Genova, Via Montallegro 1, Genova, 16143 GE, Italy

ARTICLE INFO

Keywords:
Downburst
Dynamic response
Structural monitoring
Transient event
Wind excited response

ABSTRACT

Wind excited response of structures due to downbursts has been studied using wind tunnel simulations, computational fluid dynamics applications, and analytical procedures in the previous two decades. However, the studies have not been validated with full-scale wind and structural response measurements. To fill this research gap, continuous wind-and-structural response monitoring of three slender structures was implemented through the European research council-funded project, THUNDERR. This paper focuses on one of the monitored structures, describing the monitoring system, the dynamic and aerodynamic properties, and the registered data during two downburst events. The wind-excited response of the monitored structure during two case studies of downbursts is analyzed. The correlation between the wind speed and structural displacement parameters was also studied and the square of mean wind speed was found to be highly correlated with the mean displacement and the standard deviation of the fluctuating displacement. The fluctuating components of wind speed and top displacement were found to be partially correlated. The simplicity of the selected structure, and the possibility of obtaining both the quasi-steady and resonant components of the structural response from strain registrations, will make this study a benchmark for the validation of methods and simulations of downburst wind load.

1. Introduction

Wind engineering has shown a clear advancement in the design of structures to synoptic winds after Alan G. Davenport's breakthrough framework of wind load estimation for structures through the famous Davenport chain in 1961. This framework was outlined considering synoptic winds, in which the mean and fluctuating components of the wind speed can be separated through a time average of 10 min to 1 h resulting in a constant mean and an approximately stationary Gaussian fluctuation. For many years, this has been the basis for the design criterion of wind in all codes of practice. In previous years, small-scale wind events that form due to convective activities such as tornadoes and downbursts have resulted in devastating outcomes. However, contrary to synoptic winds, design guidelines that are collectively agreed upon by researchers are not available for these transient events. A downburst is one of the small-scale meteorological events in which a downdraft of air impinges on the earth's surface creating a radial outflow (Fujita, 1985). In the past 20 years researchers have been trying to simulate downburst winds in wind tunnels (Chay and Letchford, 2002; Letchford et al., 2002; Mason et al., 2005; McConville et al., 2009; Jesson et al., 2015a,b; Romanic et al., 2019; Junayed et al., 2019; Le and Caracoglia, 2019; Asano et al., 2019; Wu et al., 2021) and in the framework of computational fluid dynamics (CFD) (Chay et al., 2006; Kim and Hangan, 2007; Sengupta et al., 2008; Vermeire et al., 2011; Aboshosha et al., 2015; Iida and Uematsu, 2019). On the other hand, researchers also proposed and applied analytical methods for the estimation of wind response during downbursts (Choi and Hidayat, 2002; Chen and Letchford, 2004; Holmes et al., 2005; Chen, 2008; Kwon and Kareem, 2009; Solari et al., 2015b; Roncallo and Solari, 2020). However, the proposed simulations and analytical methods were not validated with full-scale wind and structural response measurements during a downburst. Full-scale monitoring is essential to check whether the simplifying assumptions considered in the proposed downburst wind load modeling are acceptable and to see if all governing parameters have been given sufficient importance in the proposed models. There is a major advancement in the collection of downburst wind speed data through a network of closely spaced anemometers (Repetto et al., 2017; Solari et al., 2020), but the collection of simultaneous measurement of wind and structural response data is very rare.

Stengel and Thiele (2017) presented the first study conducted through full-scale monitoring of a structural response during a downburst. They studied the sway angle of an overhead transmission line during a downburst using full-scale wind and structural response monitoring. They have shown that the time-varying mean sway angle of the transmission line estimated using time domain analysis and

* Corresponding author.
E-mail addresses: mekdestadesse.mengistu@edu.unige.it (M.T. Mengistu), Andrea.orlando@edu.unige.it (A. Orlando), repetto@dicca.unige.it (M.P. Repetto).

https://doi.org/10.1016/j.jweia.2023.105447
Received 17 September 2022; Received in revised form 21 February 2023; Accepted 8 May 2023

registered by the monitoring system are in close agreement with each other. Lombardo et al. (2018) studied the aerodynamics of a low-rise building during the downburst event of June 2003 using full-scale pressure measurement on the walls and roof of a monitored building at Texas Tech University. They compared the loading characteristics during the downburst event with data of the same building in the previous 128 Atmospheric boundary layer (ABL) wind events. It was indicated that the observed pressure coefficients are generally below the threshold measured during ABL winds. Recently, Zhang et al. (2022) presented a study on an ultra-long stay cable during a transient event using full-scale data registered by a structural health monitoring system.

Full-scale monitoring of simple slender structures, whose aerodynamic and structural properties are relatively simple for validation with proposed downburst wind load models, is not available in the literature. To address this gap, the research group working on wind engineering at the University of Genova has initiated a full-scale structural monitoring campaign targeted at registering simultaneous wind and structural response data for three simple slender structures through the European Union-funded project, THUNDERR (Solari, 2020). The ultimate goal of the monitoring campaign is to register simultaneous measurement of downburst wind and structural response data of slender structures whose properties are relatively simple for the calculation of wind response.

This paper is a part of this wide research program. The main scope of the work is to introduce one of the three monitored structures, a slender lighting pole, and to present and discuss its response during two downburst events. The relative simplicity of the structure in terms of structural properties and geometry makes it suitable for future validation studies. The location, geometry, installed sensors, dynamic proprieties, and aerodynamic properties of the monitored structure are explained in Section 2. The procedure that has been followed to extract downburst events from the recorded wind data is described in Section 3. The selected case studies of downbursts along with the registered wind and structural response data are presented in Section 4. The wind and structural response data are discussed and analyzed in Section 5. Finally, conclusions are made and prospects for future research are recommended in Section 6.

2. Monitoring system

2.1. Description of the monitoring system

The selected structure for the wind and structural response monitoring is a 16.6 m-high lighting pole located at the harbor of La Spezia, Italy (Fig. 1). The pole is founded on a 2.5 m concrete cube, resulting in an almost perfectly fixed end connection allowing no rotation and translation at the base. The structure is made of two hollow steel shafts positioned end to end. At the junction there is a 1 m overlap where the upper shaft fits over the lower shaft, ensuring a secure connection. Both steel shafts are made through the lamination and calendaring process of a 4 mm thick steel sheet, longitudinally welding the edges of the steel sheets to create a 16-sided hollow polygon section. The bottom shaft starts from the base and extends 7.75 m. It decreases its maximum dimension from 528 mm at the base to 400 mm at the top. The upper shaft starts from 6.75 m above the base of the pole and extends to 16.6 m. It decreases its largest dimension from 417 mm at the bottom to 254 mm at the top. A steel ladder is attached to the pole along the height of the structure on one of the sides of the polygonal shaft and it is interrupted by a rectangular platform at 10 m. At the top of the pole, a square platform houses the anemometer, lighting equipment, and a security camera. In addition to its self-weight, the pole supports, the attached ladder of mass ≈ 180 kg/m, the intermediate platform of mass ≈ 60 kg, and the top platform with the lighting accessories of mass ≈ 500 kg.

The pole is equipped with a monitoring system for long-term continuous simultaneous measurement of wind and structural response. A triaxial ultrasonic anemometer measuring wind speed at a sampling frequency of 10 Hz is installed at 21.7 meters above the ground. The structural response is recorded by accelerometers and strain gauges. Two biaxial accelerometers measuring acceleration at a sampling frequency of 200 Hz are installed on one of the sides of the polygonal shafts at 11 m and 16.6 m from the base of the pole. Eight monoaxial strain gauges measuring strains at a sampling frequency of 100 Hz are installed at 0.5 m and 1.5 m above the base of the pole on 4 sides of the polygonal shaft. The strain gauges and accelerometers are placed on the sides of the polygonal shaft in such a way that response is measured in two orthogonal directions. The monitoring system has been registering wind and structural response data since February 2019 continuously except for periods of interruption due to technical problems. Until the submission of this paper, a total of 4230 h of data has been recorded.

2.2. Dynamic properties of the structure

Modal frequencies, modal shapes, and damping ratios are some of the parameters that dictate the dynamic response of any structure. Thus, quantifying these parameters was the first important step to interpreting the registered response of the monitored structure.

Forced vibration test and operational modal analysis are the two widely applied methods to obtain the dynamic properties of structures in structural response monitoring. In recent years, operational modal analysis (OMA) methods had major use in dynamic characterization because they can be applied without the need for mechanically vibrating the structure. These OMA methods use the registered response of the structure in ambient conditions to obtain the required dynamic properties. In this study, OMA methods such as the random decrement technique, frequency domain decomposition, and peak-picking method are used.

The modal frequencies were found by plotting the power spectral density (PSD) of 4-hour strain measurement using the Welch method (Welch, 1967) with 16384 points and 50% overlap. The frequencies at which the plot of PSD of strain exhibits peaks were identified as modal frequencies. Figs. 2 (a) and (b) show the PSD of strain registered by strain gauge ε_A and strain gauge ε_B in which the modal frequency of the structure can easily be observed. It can be noted that the first 2 modes are very close to each other at frequencies of 0.75 Hz and 0.85 Hz. Finite element analysis of the structure showed that the first two modes are bending modes (Orlando, 2021) along two orthogonal axes. Comparing the PSD plot of orthogonal response components such as strain ε_A and ε_B (Fig. 2(a) and (b)) gives some indication about the bending axes of the first two modes. The presence of the resonant peaks at 0.75 Hz and 0.85 Hz on both plots of PSD of ε_A and ε_B indicate that the axes of bending for the first two modes are not along the axes of measurements of ε_A and ε_B. Although the pole is made of a 16-sided polygonal cross-section, the presence of a ladder and an intermediate platform attached to one of the sides of the structure altered the approximate polar symmetry. Thus, the axes of bending had to be identified for each vibration mode. For this, a trial and error procedure was applied by calculating strain on assumed axes of bending and plotting the PSD of the strain. The assumed axes were rotated until the PSD of the strain calculated on the assumed axes showed only a single peak at either 0.75 Hz or 0.85 Hz. Table 1 explains the trial and error procedure.

Following this procedure, the principal bending axes of the structure were found to be rotated 23.5° clockwise from the local reference system of response measurement, $XX-YY$, with 1st mode of bending in the Y axis at 0.75 Hz and 2nd mode of bending in the X axis at 0.85 Hz (Fig. 3).

For clarity, the different reference local coordinate systems referred to in this paper, are summarized in Table 2.

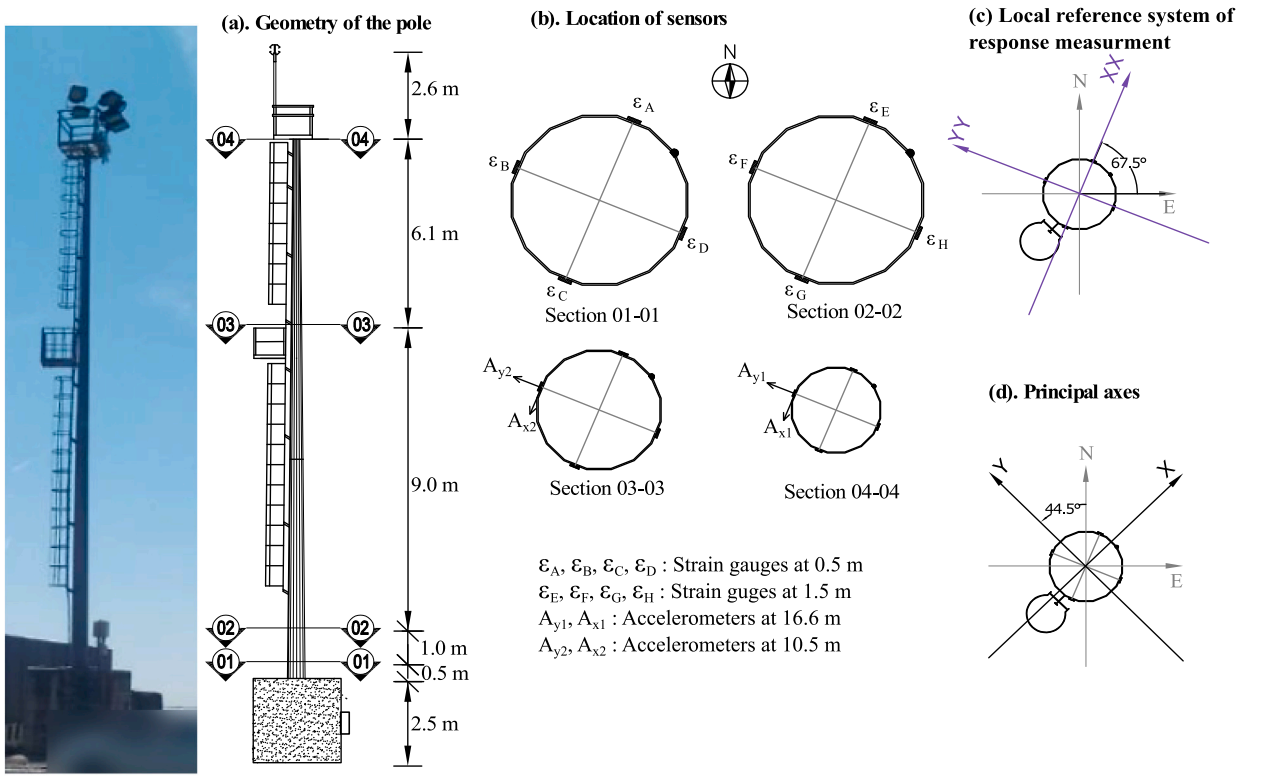

Fig. 1. The geometry of the lighting pole (a), monitoring sensor's location (b), local coordinates (XX, YY) of response measurement (c), and principal axes of the cross-section (X, Y) (d).

Table 1
Procedure of principal bending axis determination.

Step	Operation
1	Assume the bending axis corresponding to the first two modes, axes $X-Y$, to be an axis rotated by an angle γ from the measurement axes, $XX-YY$. (Fig. 3)
2	Calculate strains on points of the cross-section along axes $X-Y$, ε'_A to ε'_D, using the registered strains, ε_A to ε_D, and assuming linear strain variation under biaxial bending.
3	Plot the PSD of ε'_A to ε'_D
4	Check if only one of the resonant peaks can be spotted at either 0.75 Hz or 0.85 Hz on each of the PSDs of ε'_A to ε'_D. E.g. See Fig. 2 (c) and (d).
5	If the condition in Step 4 is satisfied, the assumed value of γ corresponds to the orientation of the first and second bending mode vibration axes. If not, E.g. See Fig. 2 (a) and (b), repeat Steps 2 to 4 changing the value of γ until the condition in step 4 is satisfied.

Estimation of modal shapes for the first two bending modes in the two principal bending directions can be done using the acceleration measurements at 10.5 m and 16.6 m. However, since the contribution of higher modes is proved to be negligible (Section 5.1), mode shapes for only the first bending modes in the two principal directions were estimated. This was done by projecting the acceleration measurement in the two horizontal directions on the principal bending axes and applying the Frequency Domain Decomposition (FDD) technique (Brincker et al., 2001; Tamura et al., 2002; Zhang et al., 2005; Brincker and Zhang, 2009). Mode shapes for the first modes in the two principal bending directions were found to be single curvature bending and they were well represented by a power function $(z/H)^k$, where z is the height above the base, H is the total height of the structure and k is a constant obtained from the FDD technique. This FDD procedure was repeated for 54 one-hour acceleration time histories to check variability in the estimation of modal shape and, as a result the mean value of the power coefficient, k, was found to be 1.9 and 1.6 with a coefficient of variation of 1.09% and 0.79% for the 1st and 2nd modes respectively.

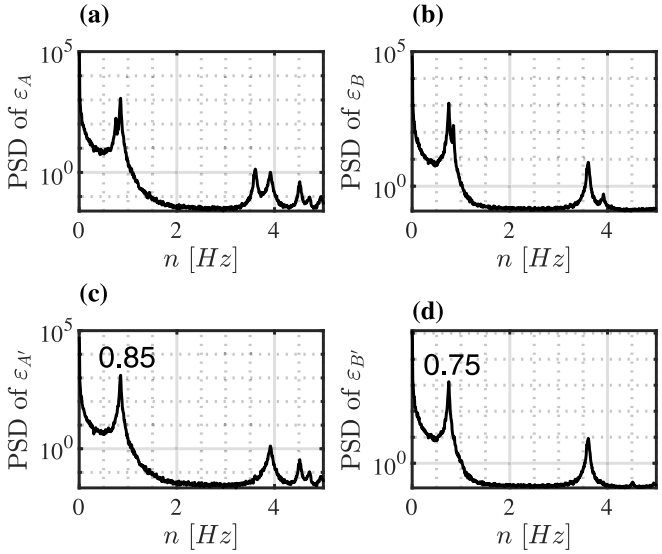

Fig. 2. PSD of strain on points along the measurement axes ((a) and (b)) and along the principal axes ((c) and (d)).

Estimation of damping ratio was attempted using three methods. The first method is the random decrement technique developed by Henry A. Cole in 1973 for detecting a failure in aerospace structures (Cole, 1973). The second and third methods stem from FDD, the difference between the two is in the procedure of extracting the damping ratio and natural frequencies from the singular values, i.e, one converts the spectral bell extracted from the singular value plot to the auto-correlation function which is generally assumed to be proportional to the impulse response function of a single degree of freedom system, FDD1 in Fig. 4, (Brincker et al., 2001) and the other fits the

Table 2
Definition of coordinate system.

Axes	Definition	Reference system
$E-N$	Global East and North axes	Geographical reference system
$XX-YY$	Axis of strain and acceleration measurement	Local reference system of response measurement
$X-Y$	Principal bending axis of the geometry for the 1st bending modes in the orthogonal directions	Principal axis reference system
$x-y$	Alongwind - crosswind direction	Local reference system of wind excited response
$d-l$	Drag and lift aerodynamic axis	Aerodynamic local reference system

Table 3
Dynamic Properties of the structure.

Mode	Natural frequency (Hz)	Mode shape		Modal mass (kg)
1st	0.75	$(\frac{z}{H})^{1.9}$	Bending in the Y direction	649
2nd	0.85	$(\frac{z}{H})^{1.6}$	Bending in the X direction	673

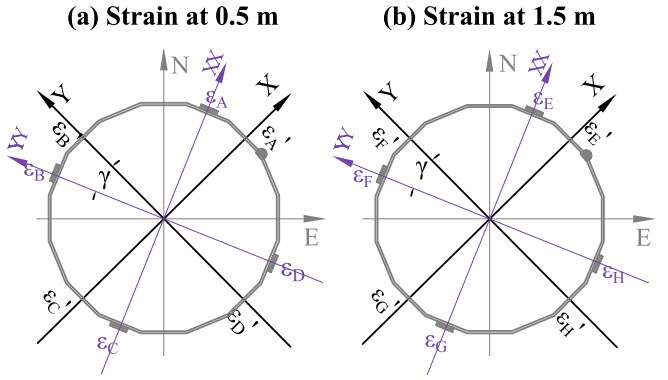

Fig. 3. Orientation of the principal axes with respect to the local reference system of strain measurement.

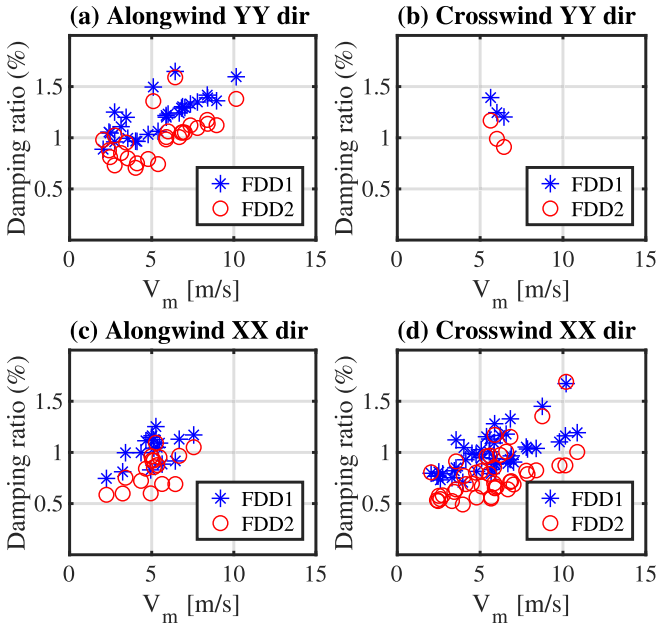

Fig. 4. Damping estimation.

frequency response function of a single degree of freedom system to the spectral bell, FDD2 in Fig. 4, (Carassale and Percivale, 2008; Pagnini et al., 2018). Damping estimates obtained from the random decrement method were not reliable because of the difficulty of extracting a sufficient length of response time history with approximately stationary wind data. Fig. 4 shows the damping ratio obtained using FDD methods using different time histories of a response corresponding to a range of mean wind speed values.

The main dynamic properties of the structure are summarized in Table 3.

2.3. Aerodynamic properties of the structure

An investigation of the aerodynamic properties of the monitored structure was carried out in the Giovanni Solari boundary layer wind tunnel at the University of Genova (https://www.gs-windyn.it/wind-tunnel/). Details of this experiment and results can be found in Orlando et al. (2023). In this section, a brief description of the wind tunnel test and its result is presented.

Three scaled models have been realized for wind tunnel experimentation. A 3D model of the top platform, 1:5 scale, reproduces all the equipment at the top of the tower: the metallic frame, the spotlights, and the security camera (Fig. 5a). Two sectional, 1:8 scale models, realized by 3D printing (Fig. 6a), represent the top and bottom segments of the tapered shaft, which has a 16-sided polygonal cross-section. They reproduce also the rounded corners, the weld, and the external ladder. As shown in Fig. 6a, the ladder can be removed to investigate its contribution to the aerodynamic forces on the pole. However in this study, to reproduce the behavior of the real structure, only results of the tests with the ladder attached are reported.

Models have been subjected to static tests to measure mean force coefficients and Strouhal number, varying angle of attack (from 0° to 360°), flow velocity (from 11 to 22 m/s), and turbulence intensity (0.2%, 3.5% and 7.5%). For each considered turbulence level, flow uniformity at the test section is under 2%. The mean force coefficients of the models have been evaluated as:

$$C_i = \frac{\bar{F}_i}{\frac{1}{2}\rho \bar{u}^2 A_{ref}} \qquad i = d, l \tag{1}$$

where $\bar{u}$ is the reference mean wind velocity (time average of the pitot measure), A_{ref} is the reference area of the models without the attachments (model diameter × tunnel width), ρ is the air density, $\bar{F}_d$ and $\bar{F}_l$, are the time-averaged aerodynamic force acting in the longitudinal and lateral directions respectively.

The mean force coefficients of the sectional models used for this work are reported in Fig. 5b and 6b. The angle of attack is measured by setting the North as 0° azimuths, while the East is 90° with subsequent values in the clockwise direction. The orientation of the section relative to the global North axis is shown in Fig. 1d. They have been obtained in turbulent flow ($I_u = 7.5\%$) with $\bar{u} = 11.0$ m/s. The considered turbulence intensity is the most compatible value with the downburst records among the turbulence levels that have been reproduced in the wind tunnel.

3. Extraction of downburst events

The main objective of this research is to study the response of the structure during downburst events. Thus, detecting the time ranges in which downburst events have occurred was the first crucial step.

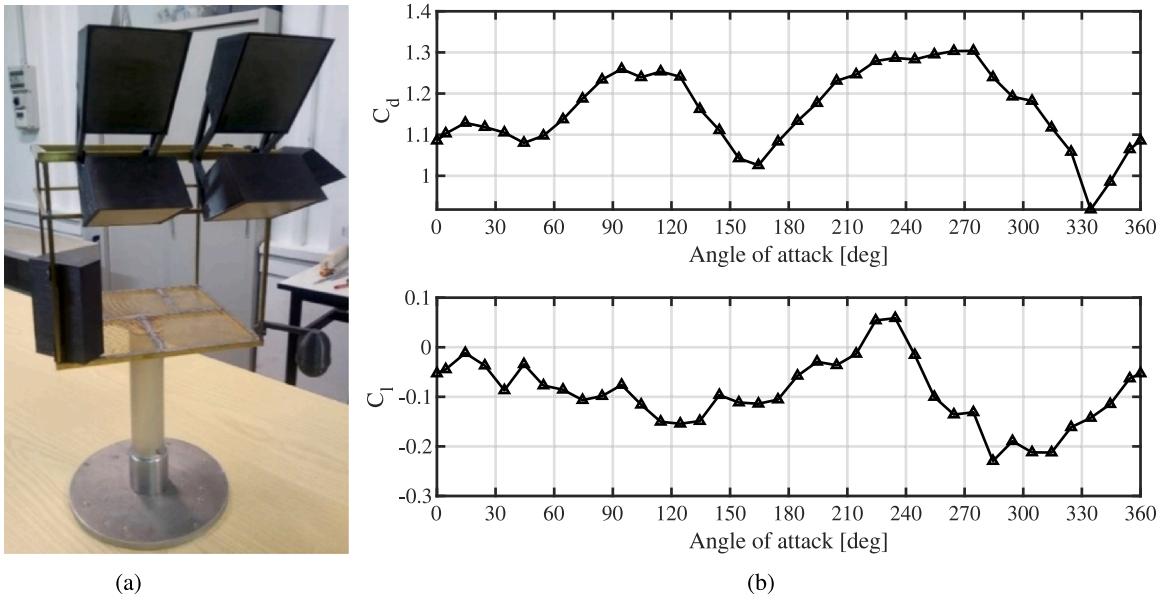

Fig. 5. 3D top platform model (a) and relevant mean force coefficients as a function of angle of attack (b). $\bar{u} = 11.0$ m/s.

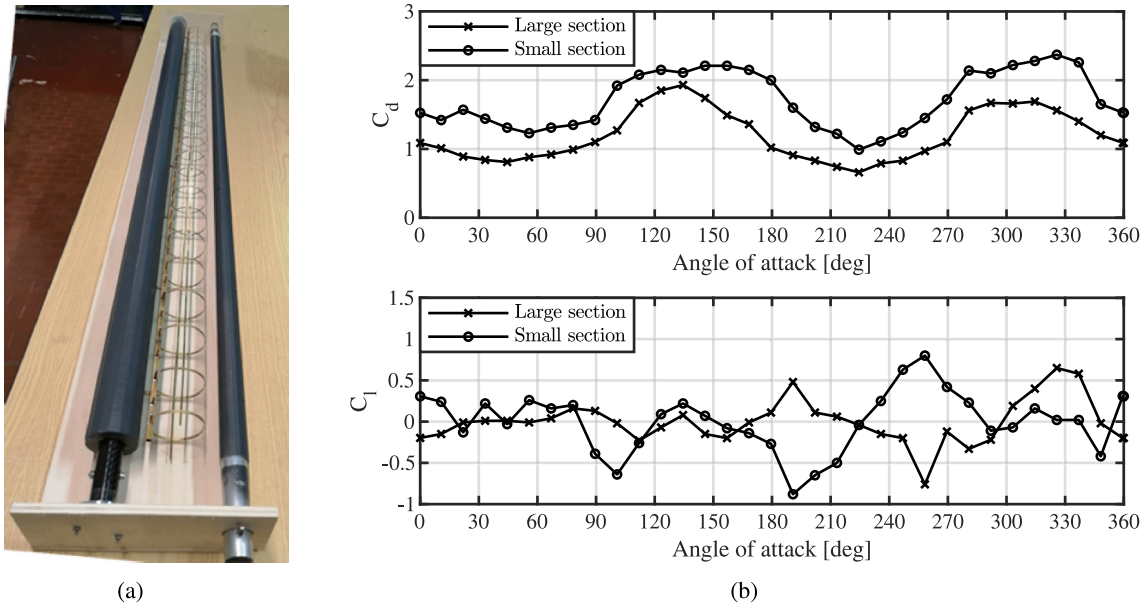

Fig. 6. Sectional models (a) and relevant mean force coefficients as a function of angle of attack (b). Turbulence intensity $I_u = 7.5\%$; $\bar{u} = 11.0$ m/s.

In previous studies, different approaches were adopted for the classification of wind events. Anemometric readings of wind speed and other meteorological indicators were used in some studies (Twisdale and Vickery, 1992; Lombardo et al., 2009; Cook et al., 2003; Huang et al., 2019). Wind speed data were used as the only basis for classification in Durañona et al. (2007) and De Gaetano et al. (2014). Wind speed data and detailed meteorological analysis were the basis of classification in Burlando et al. (2018). Since the monitored structure is not equipped with temperature, humidity, and atmospheric pressure sensors, a method proposed in De Gaetano et al. (2014) that uses wind speed data as a sole input for the classification of high-intensity winds into different categories was adopted. This method is based on the notable feature of thunderstorm winds in which a sudden increase and decrease in wind speed occur within a few minutes. This feature can be quantified using the gust factor, the ratio between the peak and the mean wind speed. For every instant of time of wind speed greater than 15 m/s, three gust factors defined in Eq. (2) were calculated.

$$G_{60} = \frac{\hat{V}_{1s}}{\bar{V}_{60}} \qquad G_{10} = \frac{\hat{V}_{1s}}{\bar{V}_{10}} \qquad G_1 = \frac{\hat{V}_{1s}}{\bar{V}_1} \tag{2}$$

where G_{60}, G_{10}, and G_1 are 1 hr, 10-minute, and 1-minute gust factors respectively; $\bar{V}_{60}$, $\bar{V}_{10}$, and $\bar{V}_1$ are 1 h, 10-minute and 1-minute averaged wind speeds respectively, and $\hat{V}_{1s}$ is peak wind speed averaged over 1 s. On the other hand, expected reference gust factors for an ABL wind at the height of the anemometer, G^0_{60}, G^0_{10}, G^0_1 were calculated using Eng. Sci. Data Unit (1985) and Solari (1993) considering the roughness at the site and the roughness changes upwind for every horizontal wind direction sector. The result is shown in Fig. 7. The calculated 1-hour and 10-minute gust factors, G_{60} and G_{10}, centered on every instant of time were compared with the expected gust factor for an ABL wind, G^0_{60} and G^0_{10}. A time instant at which the calculated gust factor falls outside a range of threshold of the expected gust factor for an ABL wind was classified as a time instant corresponding to thunder or gust

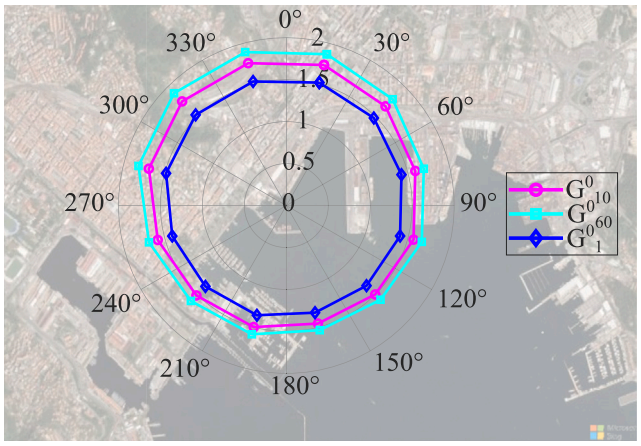

Fig. 7. Reference gust factor.

phenomenon. The range of threshold for each of the expected gust factors was adopted from De Gaetano et al. (2014). In addition, a criterion based on the ratio of the 1-minute to 10-minute gust factor was also applied according to De Gaetano et al. (2014). Events with a gust factor ratio satisfying the requirement of thunder or gust phenomena were combined as a single event provided that there are less than 4 h of a gap between them. On the other hand events with a gust factor ratio satisfying the requirement of depression events were combined as a single event provided that the time gap between them is less than 72 h. Since the wind data acquired by the anemometers is at a sampling rate of 0.1 s, an automatic algorithm was written to implement this separation procedure with minimum time. The automatic algorithm identified 20 depression events and 23 thunder or gust events. Once this quantitative separation has been done, a qualitative separation was applied by visual inspection to classify the thunder/gust wind events into the category of downburst or gust front. Through visual inspection, only two possible downburst events were found out of the 23 possible thunder/gust events.

4. Selected case studies of downburst

4.1. Wind records

Two downburst events were selected through the procedure explained in Section 3 to study the response of the structure. Fig. 8 shows 1 h time history of instantaneous wind speed, V, 10-minute running averaged wind speed, $\bar{V}_{10}$, instantaneous wind direction, α, and 10-minute running averaged wind direction, $\bar{\alpha}_{10}$, for the two events. Fig. 9 shows the 10-minute time history of instantaneous wind speed, V, 30-second running averaged mean wind speed, $\bar{V}_{30s}$, and instantaneous wind direction. Both Figs. 8 and 9 were plotted centering the maximum instantaneous wind speed. The North is set as 0° azimuths in the wind direction measurement, while the East is 90° with subsequent values in the clockwise direction.

The first event occurred on April 04, 2019, and had a maximum instantaneous wind speed of 22.5 m/s. The G_{60}, G_{10}, and G_1 values calculated at the instant of maximum wind speed are 2.2, 1.95, and 1.2 respectively. The wind direction changed from approximately 0 to 90° in about 20 min. The wind was mainly coming from the sea during the 10-minute period shown in Fig. 9. The presence of significant wind before the occurrence of the ramp-up of the downburst is due to a background ABL wind that has been present starting a couple of days before this event. After the ramp down of the wind speed, the ABL wind speed before the ramp up was not maintained.

The second event occurred on October 02, 2019, and had a maximum instantaneous wind speed of 20.5 m/s. The G_{60}, G_{10}, and G_1 values calculated at the instant of maximum wind speed are 3.65, 2.34 and 1.26 respectively. From Fig. 9 it can be observed that the wind speed increased significantly from approximately 2 m/s to 20.5 m/s in 10 min. In addition, there is a significant change in wind direction of about 180° during the ramp-up of wind speed. Similar to the first event, the wind was mainly coming from the sea during the 10-minute period shown in Fig. 9.

Table 4
Gust factor ratios calculated at time instant of maximum instantaneous wind speed.

Event	G_{60}	G_{10}	G_1	$\frac{G_{60}}{G^0_{60}}$	$\frac{G_{10}}{G^0_{10}}$	$\frac{G_1}{G_{10}}$
April 04, 2019	2.21	1.95	1.24	1.39	1.3	0.63
Oct 02, 2019	3.65	2.34	1.26	2.3	1.56	0.34

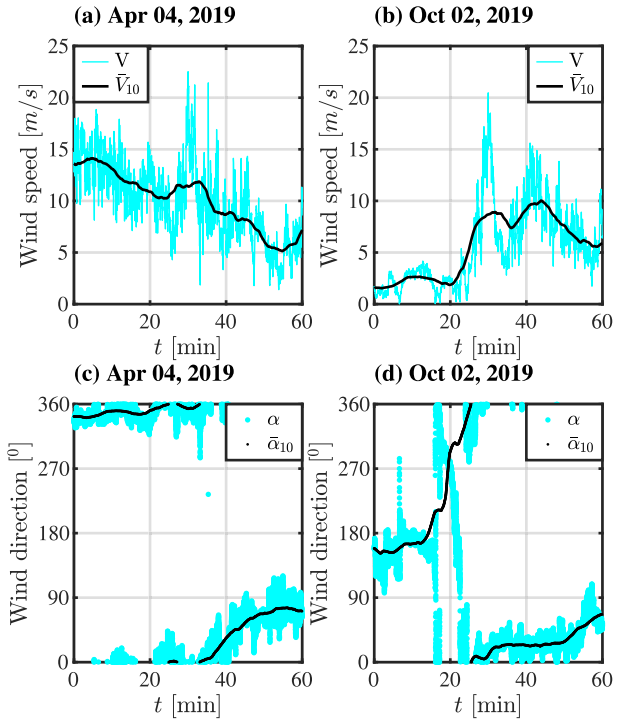

Fig. 8. 1-hour time history of wind speed ((a) and (b)), and direction ((c) and (d)) centered at the maximum wind speed for the two downbursts.

The gust factors and normalized ratios calculated at the instant of maximum wind speed for the two selected downburst events are summarized in Table 4.

4.2. Decomposition of wind speed

Decomposition of horizontal wind speed into mean and fluctuating components is a common procedure in synoptic winds to study the mean static and dynamic responses of structures separately. Similarly, studies on thunderstorm winds also decomposed wind speed into slowly varying mean and fluctuating components. Contrary to the classical approach in ABL winds, the decomposition approach applied for thunderstorm winds ignored the fluctuating component in the crosswind direction. Because of this, subsequent research on the dynamic responses of structures to thunderstorm winds considered only the alongwind response and neglected the change in the angle of attack with time (Chen and Letchford, 2004; Choi and Tanurdjaja, 2002; Kwon and Kareem, 2009; Solari et al., 2015b, 2017; Solari, 2016). Zhang et al. (2019) proposed a new approach, referred to as directional decomposition, in which the wind speed is decomposed into slowly varying mean and fluctuating components in the alongwind direction, and fluctuating components in the crosswind direction. This enabled

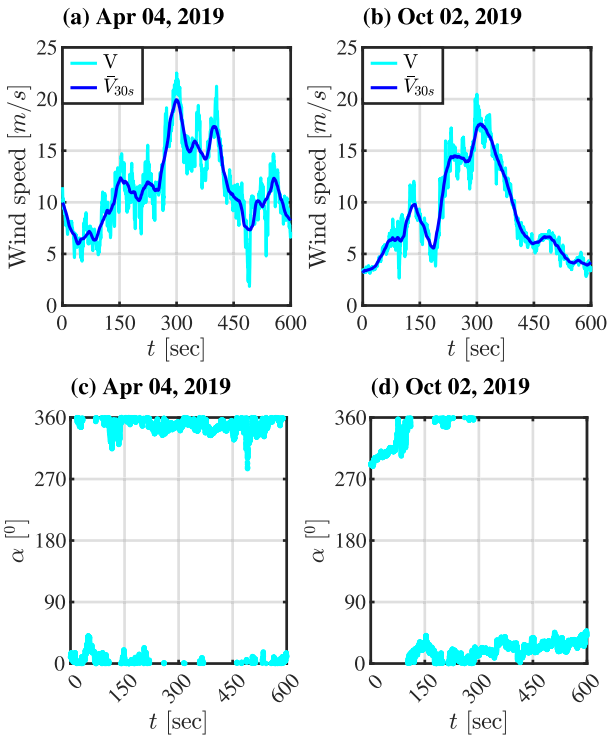

Fig. 9. 10 min time history of wind speed ((a) and (b)), and direction ((c) and (d)) centered at the maximum wind speed for the two downbursts.

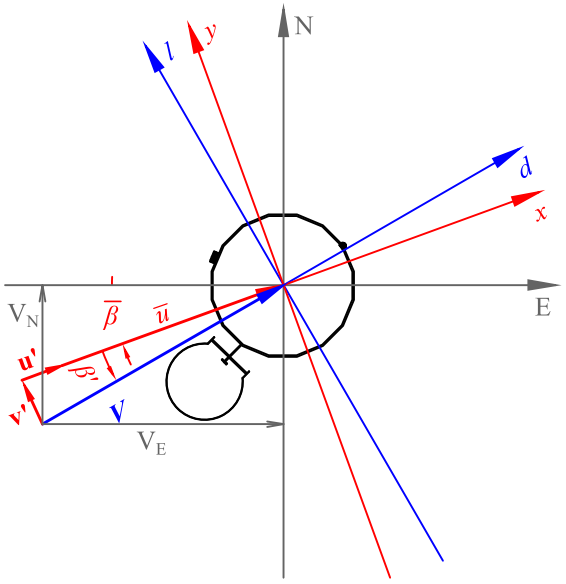

Fig. 10. Directional decomposition of wind speed.

Table 5
Main features of wind speed for the two events.

Event	$\bar{u}(t)_{\max}$ (m/s)	$\sigma_u(t)_{\max}$ (m/s)	$\sigma_v(t)_{\max}$ (m/s)	$I_u(t)_{mean}$ (-)	$I_v(t)_{mean}$ (-)
April 04, 2019	19.9	2.64	2.6	0.13	0.11
Oct 02, 2019	17.6	1.69	1.59	0.09	0.09

the estimation of alongwind and crosswind responses and consideration of the change in the angle of attack (Brusco et al., 2019). Hence, this approach was used to decompose wind speed for the two downburst events considered in this study.

Following the procedure defined in Solari et al. (2015a), a preliminary analysis has been made, to select the most convenient time averaging. In particular, the slowly varying mean was calculated using 10, 20, 30, and 40-second averaging windows, and the frequency contents of the slowly varying mean and of the fluctuating components were evaluated. The results showed that, for the two considered events, 30 s is the averaging window that best separates the two harmonic contents.

The directional decomposition technique is illustrated in Fig. 10. First slowly varying mean wind speeds averaged over 30 s, $\bar{V}_E(t)$ and $\bar{V}_N(t)$, are extracted from the instantaneous wind speed registered in the East and North directions, $V_E(t)$ and $V_N(t)$, respectively. After the mean extraction, the residues are the fluctuating components, V'_E and V'_N.

$$V_E(t) = \bar{V}_E(t) + V'_E(t) \tag{3}$$

$$V_N(t) = \bar{V}_N(t) + V'_N(t) \tag{4}$$

The mean wind speed components, $\bar{V}_E$ and $\bar{V}_N$, are vector summed to obtain the resultant slowly varying mean wind speed, $\bar{u}(t)$, and its direction, $\bar{\beta}(t)$.

$$\bar{u}(t) = \sqrt{\bar{V}_E^2(t) + \bar{V}_N^2(t)} \tag{5}$$

$$\bar{\beta}(t) = \arctan 2\left[\frac{\bar{V}_N(t)}{\bar{V}_E(t)}\right] \tag{6}$$

where $\arctan 2$ is the four-quadrant inverse tangent.

The remaining fluctuating components, $V'_E(t)$ and $V'_N(t)$, are projected on new orthogonal axes, $x-y$, in which x-axis is aligned with $\bar{u}(t)$.

$$u'(t) = V'_E(t)\cos\bar{\beta}(t) + V'_N(t)\sin\bar{\beta}(t) \tag{7}$$

$$v'(t) = -V'_E(t)\sin\bar{\beta}(t) + V'_N(t)\cos\bar{\beta}(t) \tag{8}$$

The alongwind and crosswind fluctuating components, $u'(t)$ and $v'(t)$, are further decomposed as a product of their standard deviation, $\sigma_u(t)$ and $\sigma_v(t)$, and rapidly varying stationary-Gaussian components, $\tilde{u}'(t)$ and $\tilde{v}'(t)$.

$$u'(t) = \sigma_u(t)\,\tilde{u}'(t) \tag{9}$$

$$v'(t) = \sigma_v(t)\,\tilde{v}'(t) \tag{10}$$

Thus, the alongwind and crosswind components of the wind speed are expressed as:

$$u(t) = \bar{u}(t) + u'(t) = \bar{u}(t)\left[1 + I_u(t)\,\tilde{u}'(t)\right] \tag{11}$$

$$v(t) = v'(t) = \bar{u}(t)\,I_v(t)\,\tilde{v}'(t) \tag{12}$$

where $I_u(t) = \sigma_u(t)/\bar{u}(t)$ and $I_v(t) = \sigma_v(t)/\bar{u}(t)$ are the longitudinal and lateral slowly varying turbulence intensities. $u(t)$ and $v(t)$ can be vector summed to get the resultant wind speed $V(t)$ which results in drag and lift forces parallel and perpendicular to it, along aerodynamic axes $d-l$ shown in Fig. 10.

Figs. 11 and 12 show the 10-minute time history of components of wind speed and wind direction obtained through directional decomposition for the two events studied in this paper. The 10-minute time history was extracted centering the time instant at which the resultant wind speed is maximum. The main features of the wind speed components are summarized in Table 5.

4.3. Top displacement from strain

Although the monitoring station is equipped with both accelerometers and strain gauges, the strain gauge readings were better at capturing the response because both the quasi-steady and resonant components of the response can be obtained from the strain gauge readings

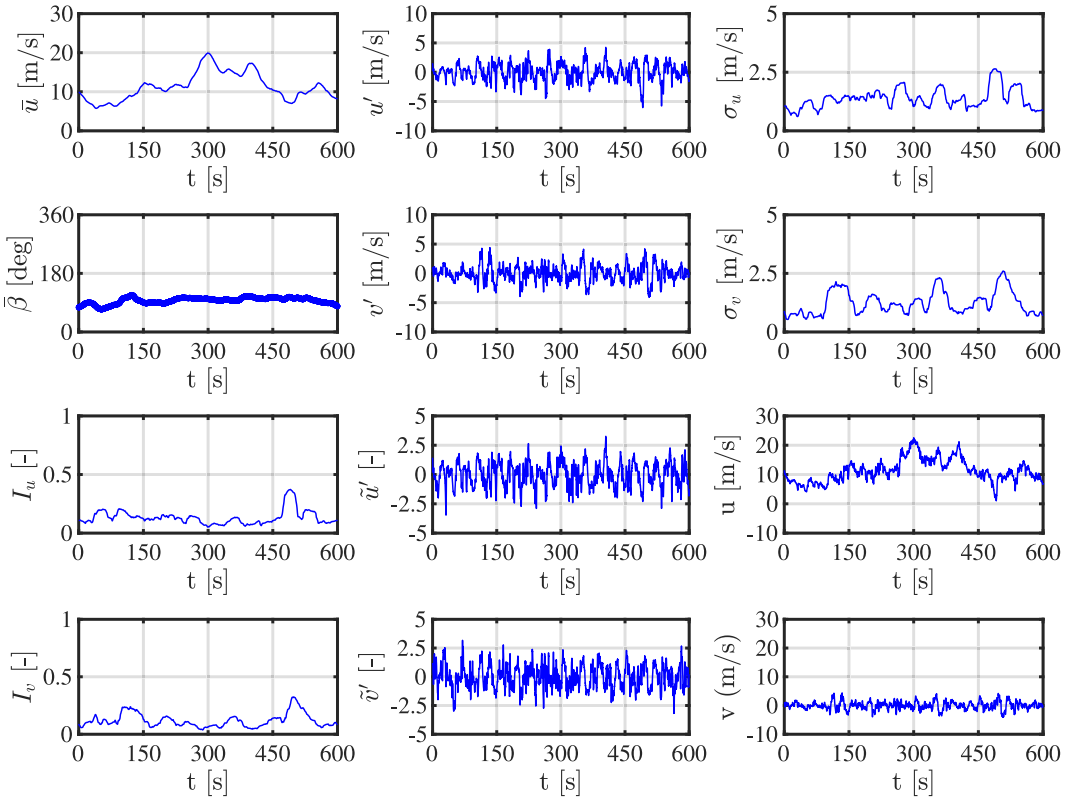

Fig. 11. Decomposition of wind speed for the downburst event on Apr 04, 2019.

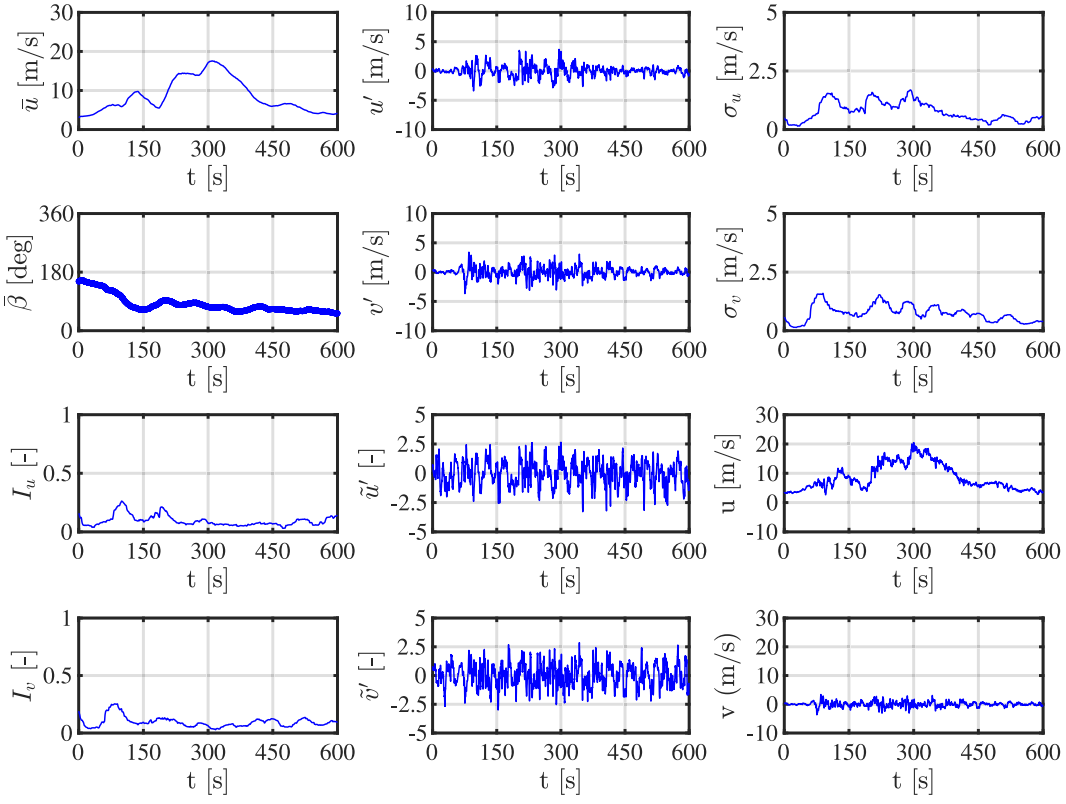

Fig. 12. Decomposition of wind speed for the downburst event on Oct 02, 2019.

while the quasi-steady part of the response is unreliable in the accelerometer readings. This is because of the inherent properties of the strain gauges and accelerometers, where the strain gauges register the strain due to both the low and high-frequency vibrations while the accelerometers do not register the low-frequency component of the vibration. Thus, part of the low-frequency component of the quasi-steady vibration is not registered by the accelerometers.

Initially, the strain gauge readings had to be calibrated to have a zero-strain measurement when there is no wind load exerted on the structure. The calibration had to be done for each event separately because of the inherent property of strain gauges, in which the resistance changes in time (long-term drift). For this calibration, the time instant, t_s, at which wind speed is almost zero in the previous 2 - 72 h before the downburst event, had to be found. Once this time instant, t_s, is found for each of the downburst events, the strain measurement of each strain gauge at t_s was identified as the strain shift. This strain shift was subtracted from each strain gauge readings, to obtain the correct strain value.

As shown in Fig. 1, there are 8 strain gauges registering strain at two different heights of the structure. Since strain due to axial load in the structure is not part of the registered strain, the strain gauge readings can safely be assumed to be the result of pure biaxial bending resulting from the lateral wind load. In addition, the two locations at which the strain gauges are attached to the surface of the structure, are below the vertical ladder attached to the pole and as a result, the cross-section is approximately polar symmetric. Thus, the strains measured by strain gauges installed on the opposite faces of the cross-section are expected to have a similar magnitude of tension and compression strain.

With the assumption of pure biaxial bending, the deflection of the structure from strain gauge readings can be obtained by applying the Bernoulli–Euler beam equation for small deflection:

$$\frac{d^2\delta(t,z)}{dz^2} = \frac{M(t,z)}{EI(z)} \tag{13}$$

where δ is deflection; z is height; M is bending moment; I is area moment of inertia; and E is elastic modulus.

From flexure theory, $M(t,z) = S(t,z)\,I(z)/r(z)$, where S is flexural stress and r is the distance from the centroid of the cross-section to the outermost point. Assuming the section to be linearly elastic, Hook's law can be applied, and flexural stress can be expressed as a product of strain, $\varepsilon(t,z)$ and modulus of Elasticity, E.

$$M(t,z) = \frac{\varepsilon(t,z)\,EI(z)}{r(z)} \tag{14}$$

Assuming the defection to have resulted from only the 1st mode single curvature bending, it can be defined as a product of the principal coordinate of deflection, $P_{1,i}$, and modal shape, $\psi_{1,i}(z)$.

$$\delta_i(t,z) = P_{1,i}(t)\,\psi_{1,i}(z) \qquad i = X, Y \tag{15}$$

substituting Eq. (14) and Eq. (15) in Eq. (13),

$$P_{1,i} = \frac{\varepsilon(t,z)}{r(z)\,\frac{d^2\psi_{1,i}(z)}{dz^2}} \qquad i = X, Y \tag{16}$$

As discussed in Section 2.2, the structure is not polar symmetric and the first two modes are single curvature bending about the two orthogonal directions X and Y. Thus the resultant deflection of the structure should be the vector sum of deflections in the X and Y directions. To obtain the principal coordinate of deflection in the X and Y directions, first, strains at the outermost points of the cross-section in the two principal directions have to be calculated. These strains, ε'_A to ε'_H, were calculated from the available sets of strain measurements, ε_A to ε_H, assuming a linear strain distribution with zero strain at the centroid of the section and maximum strain at the outermost surface (Fig. 3). In the strain registration, tensile strain is positive, and compressive strain is negative.

Using Eq. (16), strains, ε'_A, ε'_C, ε'_E, ε'_G, were used to calculate the principal coordinate of deflection in the X direction, $P_{1,X}(t)$, and strains, ε'_B, ε'_D, ε'_F, ε'_H, were used to calculate the principal coordinate of deflection in the Y direction, $P_{1,Y}(t)$.

$r(z)$ is 257.9 mm at $z = 0.5$ m from the base of the structure where strain gauges ε'_A to ε'_D are installed and $r(z)$ is 249.65 mm at $z = 1.5$ m from the base of the structure where strain gauges ε'_E to ε'_H are installed. Since the 1st bending modal shape was approximated by a power function, its second derivative is,

$$\frac{d^2\psi}{dz^2} = k(k-1)\left(\frac{z}{H}\right)^{k-2}\frac{1}{H^2} \tag{17}$$

Figs. 13 and 14 show the time history of top displacements in the X and Y directions calculated using strains ε'_A to ε'_H for the two case studies of downbursts. Sub-figures (a) and (b) show the top displacements in the X and Y directions. Sub-figure (c) shows the polar plot of the resultant displacement obtained using all the possible pairs of orthogonal strains. Sub-figures (d) and (e) show the running mean top displacements averaged over 30 s, $\bar{X}$ and $\bar{Y}$, that are extracted from the top displacement obtained using each strain record, X and Y. The averaging time for the running mean top displacement is selected to be 30 s for consistency with the running mean wind speed. Sub-figures (f) and (g) show the residual fluctuating top displacements, $X\prime$ and $Y\prime$, that are obtained by subtracting the running mean top displacements, $\bar{X}$ and $\bar{Y}$, from the total top displacements, X and Y. Sub-figures (h) and (i) show the time-varying standard deviations of the fluctuating top displacement, σ_X and σ_Y, that are obtained by calculating the running standard deviations of the residual fluctuation over 30 s. Table 6 summarizes the ensemble mean values and standard deviations of maximum top displacement parameters obtained using the eight strain gauges. The variability between readings is high. Although tracing the cause of these variabilities is not trivial, temperature-induced effects in strain measurement and strain calibration errors could be the sources of error. Ideally, only two strain gauges oriented on orthogonal faces of the cross-section could be sufficient to measure the response but the availability of 8 strain gauges enabled us to obtain 4 displacement results in each orthogonal direction. This will be useful to compensate for the variability observed among strain gauges through averaging.

Table 6
Top displacement obtained from strain measurement.

Event	Apr 04, 2019		Oct 02, 2019	
	mean	std	mean	std
$\bar{X}_{\max}$ (cm)	1.76	0.55	2.77	0.67
$\bar{Y}_{\max}$ (cm)	5.28	0.41	2.52	0.24
$X\prime_{\max}$ (cm)	2.97	0.78	2.31	0.61
$Y\prime_{\max}$ (cm)	4.27	0.37	2.36	0.20
$\sigma_{X\max}$ (cm)	0.98	0.26	0.83	0.22
$\sigma_{Y\max}$ (cm)	1.42	0.13	0.90	0.08

4.4. Top displacement from acceleration

The monitored structure is equipped with accelerometers at two heights. The accelerometer at 10.5 m was working during both of the selected downburst events but the accelerometer at 16.6 m was not working during the downburst event on October 02, 2019. Although the accelerometer at 16.6 m is expected to have a better amplitude-to-noise ratio for the analysis of the first bending modes, an acceleration measurement at 10.5 m is also sufficient to derive the structural response for the first vibration modes in the two principal bending directions.

The high-frequency component of the response is expected to be satisfactorily registered by the accelerometers while the low-frequency quasi-steady component is expected to be erroneous due to the inherent property of the accelerometers. Although the strain gauges are expected to capture both the quasi-steady and resonant parts of the response, analysis of the acceleration measurement is important to validate the strain measurements and to check if all the important frequency components were captured by the strain gauges. Thus, the

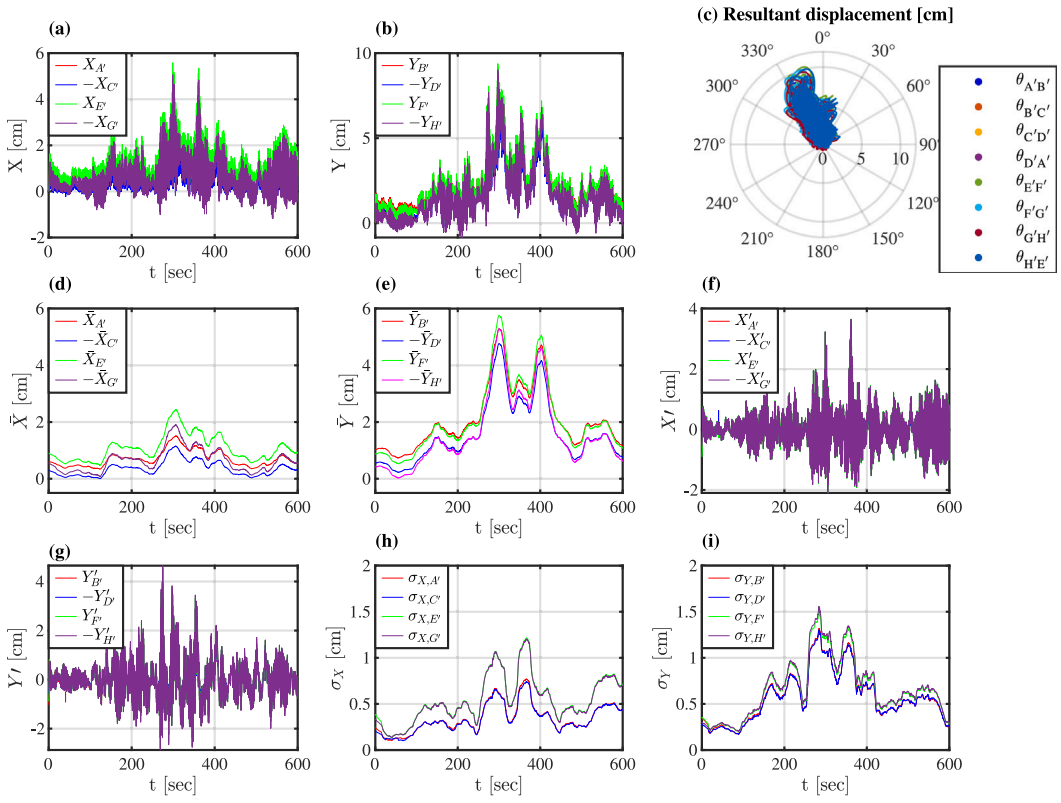

Fig. 13. Top displacement calculated using strain registrations ((a) and (b)), resultant (c), mean part ((d) and (e)), fluctuating part ((f) and (g)), and standard deviation of the fluctuating part ((h) and (i)) for the downburst on April 04, 2019.

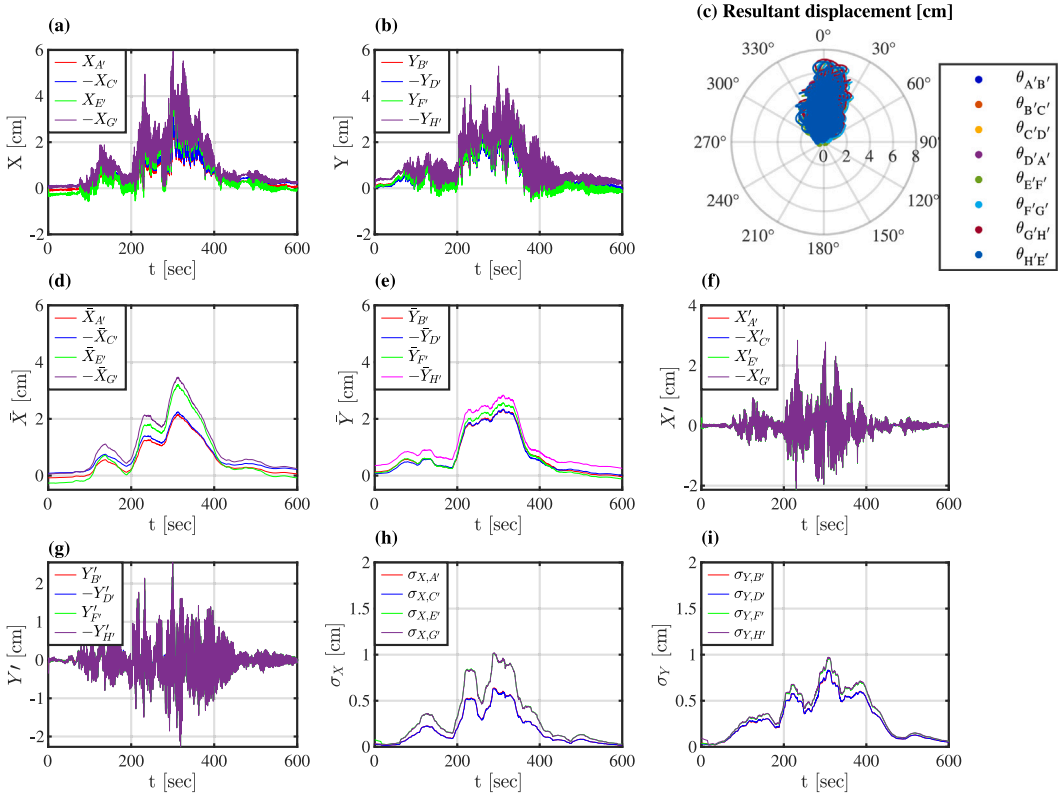

Fig. 14. Top displacement calculated using strain registrations ((a) and (b)), resultant (c), mean part ((d) and (e)), fluctuating part ((f) and (g)), and standard deviation of the fluctuating part ((h) and (i)) for the downburst on October 02, 2019.

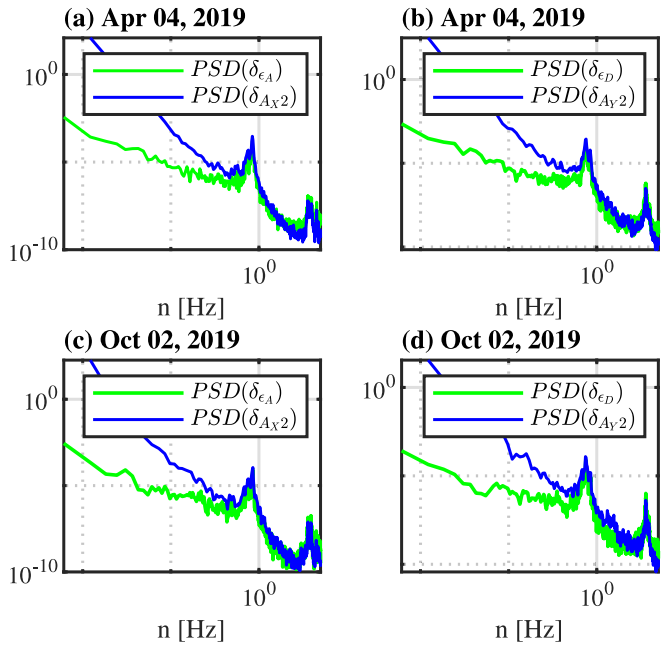

Fig. 15. PSD of displacement in the XX and YY direction at 11 m obtained from strain and acceleration.

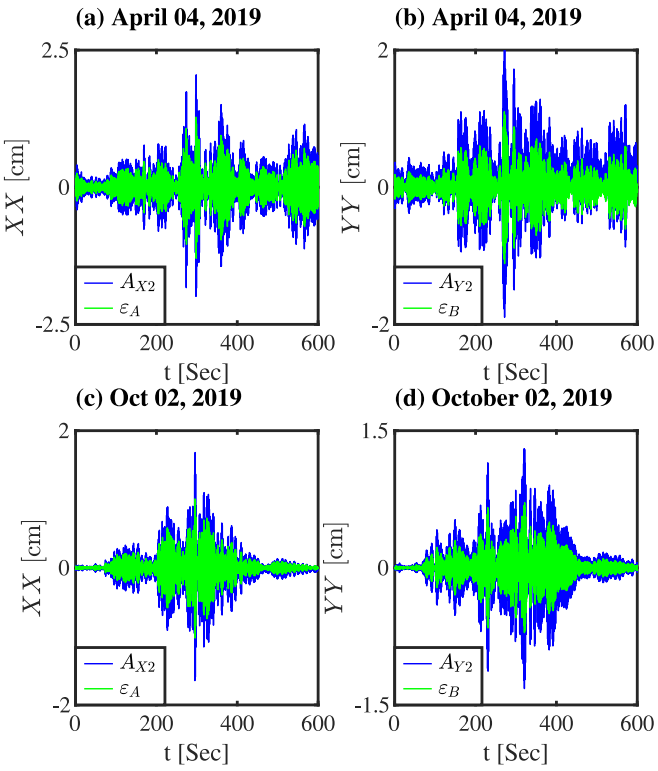

Fig. 16. Top displacement obtained from strain and acceleration.

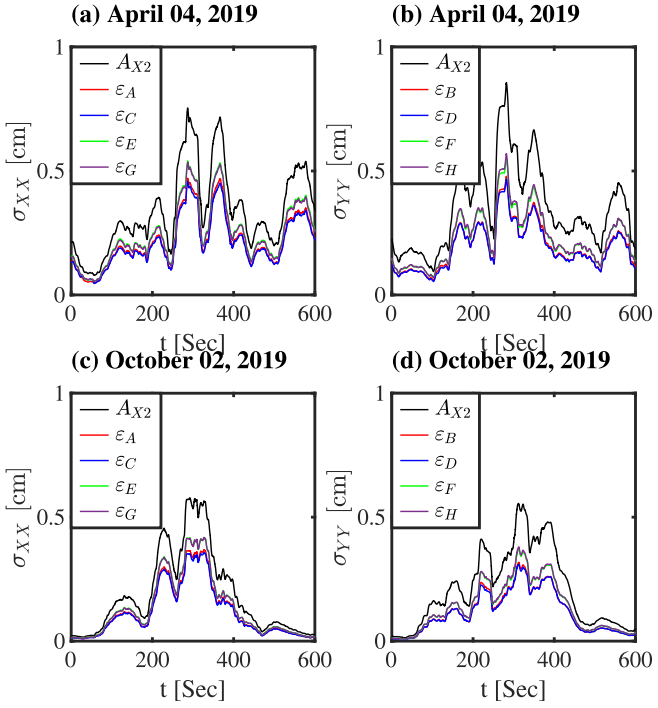

Fig. 17. Standard deviation of fluctuating top displacement obtained from strain and acceleration.

fluctuating component of the displacement of the structure had to be calculated from the acceleration measurements and compared with the result obtained from strain gauges. The comparison was initially done in the frequency domain by plotting the PSD of displacement at 10.5 m obtained from strain measurement and the PSD of displacement at 10.5 m obtained by dividing the PSD of acceleration by ω^4, where ω is the circular frequency. Since the process is not stationary, the comparison was done carefully by calculating the PSD of both results considering similar segment length and overlapping through the Welch method. Fig. 15 shows a comparison made between results of strain ϵ_A and ϵ_D with results of acceleration A_{X2} and A_{Y2} for the two selected downburst events. As expected, the two results are not matching in the low-frequency region representing the quasi-steady response but the results are comparable near the first and second mode frequencies, 0.75 Hz and 0.85 Hz. In general, the results of acceleration appear to be slightly higher than the results of strain for the first two bending modes but the reverse is true for higher frequencies.

In theory, displacement can be calculated from acceleration through double integration. However, in reality, this calculation is not trivial because of the unknown initial conditions and the presence of noise. Integration of an acceleration measurement with noise, to obtain velocity or displacement usually results in a drift, requiring attention in numerical applications. In this study, a rigorous procedure was applied to avoid drift and minimize sources of errors. Initially, the acceleration measurement was bandpass filtered between 0.6 and 1 Hz to remove noise. Then, double integration was applied numerically to calculate the displacement. Finally, a high pass filter with a pass band frequency of 0.6 Hz was applied to remove the resulting drift. In Fig. 16, the displacement at 10.5 m obtained using strain gauges, bandpass filtered between frequencies of 0.6 and 1 Hz, is compared with the displacement obtained from double integration of acceleration for strains and accelerations ϵ_A, ϵ_B, A_{X2} and A_{Y2}. For better comparison, the running standard deviation of the displacement averaged over 30 s, σ_{XX} and σ_{YY} were calculated for the displacement obtained from each strain gauge and acceleration. The result is presented in Fig. 17. Although the general trend of the time history of displacement fluctuation is similar, it can be noted that the displacement obtained from acceleration registrations is always higher than the one obtained from strain registrations. Possible causes of this discrepancy could be instrumentation or calibration error in either of the two measurements.

5. Discussion

5.1. Contribution of higher modes

In wind engineering, it is common to consider only the first few modes of vibration for the analysis of the dynamic amplification of

Table 7
Contribution of first mode vibration.

Event	$\epsilon_{A'}$	$\epsilon_{B'}$	$\epsilon_{C'}$	$\epsilon_{D'}$	$\epsilon_{E'}$	$\epsilon_{F'}$	$\epsilon_{G'}$	$\epsilon_{H'}$
April 04, 2019	92.8%	87.9%	84.2%	90.6%	93.9%	92.6%	93.8%	92.6%
Oct 02, 2019	92.5%	86.6%	92.0%	86.8%	93.5%	87.7%	93.4%	88.0%

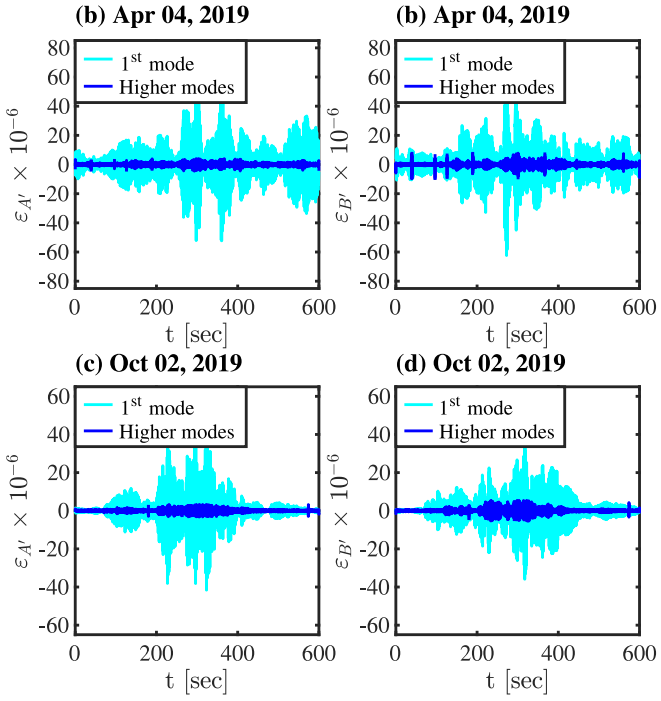

Fig. 18. Comparison between the contribution of 1st mode and higher mode.

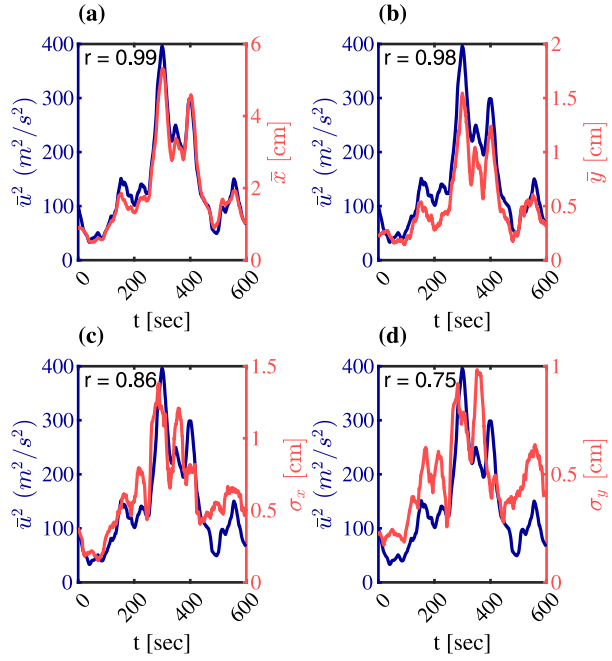

Fig. 19. Relationship between mean wind speed (blue) and top displacement (red) for the event on April 04, 2019.

displacement of the structure due to the turbulent wind. Similarly, in this study, only the first vibration modes in the two orthogonal principal bending directions were considered assuming the contribution of higher modes to be negligible. The contribution of higher modes was removed by lowpass filtering the strain gauge readings at a cutoff frequency of 1 Hz and by bandpass filtering the accelerometer readings between 0.6 and 1 Hz before the calculation of the structural displacement from strain and acceleration. To make sure that this assumption of negligible higher mode contribution is correct, a comparison between strain in the principal bending directions was done by separating the first mode and higher mode contributions through bandpass filtering. Fig. 18 shows an example of the comparison between the contribution of the first modes and the higher modes in the two principal bending directions on the strain $\epsilon_{A'}$ and $\epsilon_{B'}$ during the two downburst events. Although the higher mode contribution is not entirely zero, it can be observed that the amplitude is not significant in comparison to the contribution of the first mode. The contribution of the first mode vibration was calculated by dividing the maximum strain obtained after applying a lowpass filter with a cutoff frequency of 1 Hz by the maximum strain obtained after applying a lowpass filter with a cutoff frequency of 10 Hz. The result is presented in Table 7 for each strain as a percentage. In all cases, the contribution of the first mode vibration was found to be more than 85%.

5.2. Relationship between the structural response and wind speed parameters

In this section, wind speed parameters such as time-varying mean wind speed and time-varying standard deviation of fluctuating wind speed defined in Section 4.2 are compared with simultaneous structural response parameters such as time-varying mean top displacement and time-varying standard deviation of the top displacement fluctuation presented in Section 4.3. The comparison is carried out between the time histories of the selected wind and structural response parameters by calculating their correlation coefficient. The calculated correlation coefficient, r, is reported on the top left/right corner of the time history plots for each of the comparisons and it is calculated as:

$$r(A,B) = \frac{1}{N-1}\sum_{i=1}^{N}\left(\frac{A_i-\mu_A}{\sigma_A}\right)\left(\frac{B_i-\mu_B}{\sigma_B}\right) \tag{18}$$

where A and B are the two time series to be compared; μ_A and σ_A are the mean and standard deviation of A, respectively; μ_B and σ_B are the mean and standard deviation of B; N is the number of data points.

Figs. 19 and 20(a) and (b) show a plot of mean wind speed squared, $\bar{u}^2$ and mean top displacement in the alongwind and crosswind directions, $\bar{x}$ and $\bar{y}$. As can be observed from the similarity of the trend of the two plots and the value of the correlation coefficient, the alongwind response is closely correlated with the square of mean wind speed for both events. The trend of the time history of the crosswind top displacement also shows some resemblance with $\bar{u}^2$. This result was expected because, under the quasi-steady hypothesis, the aerodynamic force should be directly proportional to the square of the wind speed.

Figs. 19 and 20(c) and (d) show a time history of mean wind speed squared, $\bar{u}^2$, and the standard deviation of the fluctuating top displacement in the alongwind and crosswind direction, σ_x and σ_y. In both cases, the maximum value of the standard deviation of the top displacement fluctuation is at the vicinity of the time instant at which the mean wind speed is maximum. In addition, the general trend of the standard deviation has some similarity with the trend of the square of the mean wind speed and they are positively correlated with a correlation coefficient greater than 0.76.

Figs. 21 and 22 show the time history of mean wind speed, $\bar{u}$, multiplied by the standard deviation of wind speed fluctuations, σ_u

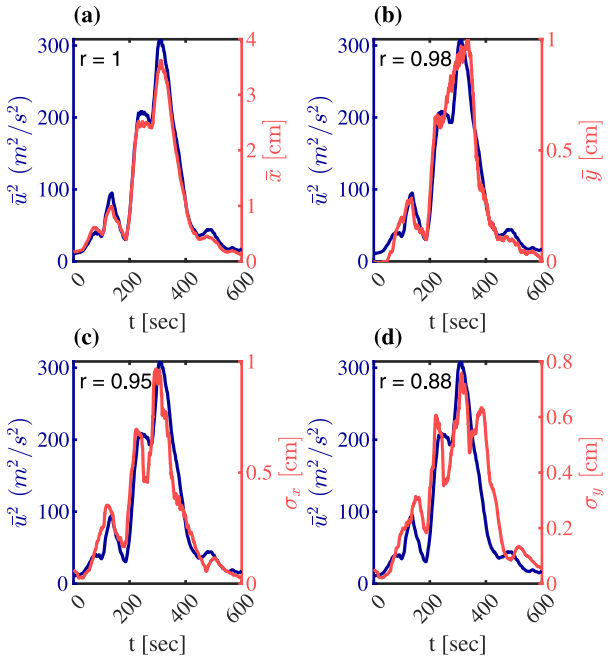

Fig. 20. Relationship between mean wind speed (blue) and top displacement (red) for the event on October 02, 2019.

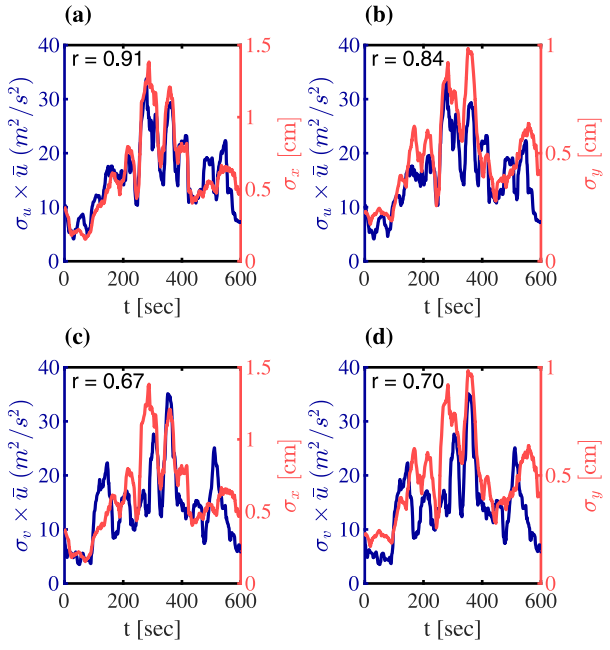

Fig. 21. Relationship between wind speed fluctuation (blue) and top displacement fluctuation (red) for the event on April 04, 2019.

and σ_v, and standard deviation of the fluctuating top displacement, σ_x and σ_y in the alongwind and crosswind direction. This comparison is based on the quasi-steady theory, in which the fluctuating part of the response is made of two contributions; one proportional to $\bar{u}u'$ and one proportional to $\bar{u}v'$, whose respective weight depends on the aerodynamic coefficients (Piccardo and Solari, 2000). The results show that the alongwind response fluctuation is always highly correlated with $\bar{u}u'$ due to the weight of C_d with respect to the other coefficients. Regarding the crosswind response, the contributions of $\bar{u}u'$ and of $\bar{u}v'$ are more balanced due to the great variability of C_l and C_l'. However, the overall high correlation values show the considerable contribution

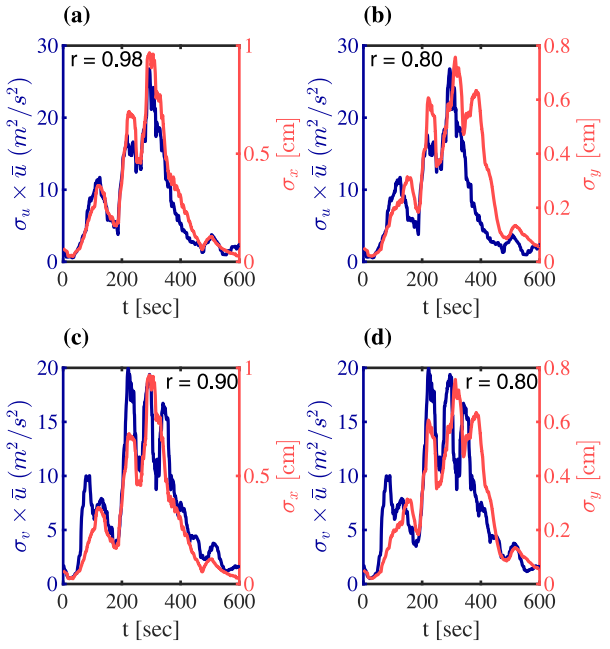

Fig. 22. Relationship between wind speed fluctuation (blue) and top displacement fluctuation (red) for the event on October 02, 2019.

of all the aerodynamic coefficients (C_d, C_d', C_l, C_l') which, except for the drag coefficient are usually disregarded for polar symmetric structures.

5.3. Relationship between wind and response direction

The direction of the structure's response was compared with the wind direction by calculating the direction of the structure's response from displacements obtained using orthogonal strains. Figs. 23 (a) and (b) show a polar plot of the normalized mean wind speed, $\bar{u}$, and its direction, $\bar{\beta}$, as well as the normalized resultant mean top displacement and its direction. On the other hand, Figs. 23 (c) and (d) show the time history of mean wind direction and mean response direction. The shift in the mean response direction relative to the mean wind direction is also shown on the same plots. Comparing polar plots of mean wind speed and mean top displacement for the event on April 04, 2019, it is evident that the mean wind direction is approximately between 330 and 0 degrees but the response shows a shift towards the northwest direction relative to the mean wind direction. A similar shift can be visually observed for the event on October 02, 2019. This shift plotted in Fig. 23(c) and (d), is varying with time and it is around 15 degrees at the time range closer to the instant of maximum wind speed, 300 s. The shift proves the lift aerodynamic effect; however, the value of the shift is not completely coherent with the lift coefficient evaluated in the wind tunnel, suggesting further research on transient aerodynamics.

6. Conclusion and prospect

This study addressed the dynamic response of a slender lighting pole whose wind and structural response were monitored simultaneously with a long-term continuous monitoring system. Initially, an automatic algorithm was written for the separation of downburst and gust winds from depressions based on the wind speed measurement. The automatic algorithm was supplemented with qualitative judgment to separate downburst and gust winds. This enabled the selection of two case studies of downbursts whose wind-and-structural responses were registered by the monitoring system. The strain and acceleration measurements during ambient conditions were used to obtain the structure's dynamic properties through operational modal analysis methods. Although the

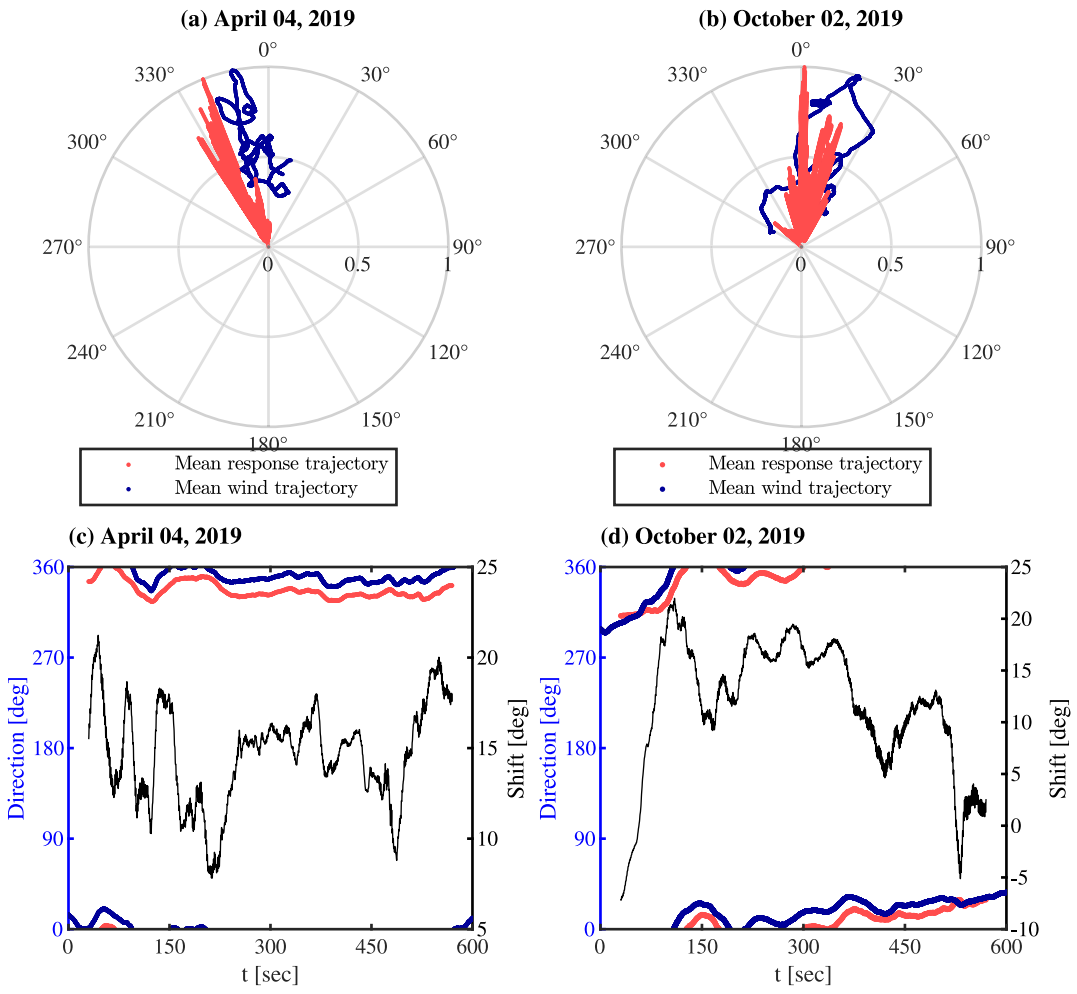

Fig. 23. Polar plot of normalized mean wind speed and normalized mean top displacement ((a) and (b)), and time history of mean wind direction and mean response direction ((c) and (d)) for the two downburst events.

modal frequencies, modal shapes, and the axis of bending were found for the modes of interest, the estimate of damping presented a large uncertainty. The time history of the displacement of the structure was estimated from the strain and acceleration measurements considering the first vibration modes of bending in the orthogonal directions. It was possible to obtain both the quasi-steady and resonant components of the displacement from strain measurements. This will be useful in future studies of the aerodynamics of similar structures under downburst winds. The contribution of higher vibration modes was studied by separating the first vibration modes in the orthogonal bending directions from the rest of the vibration modes and comparing the maximum response in both cases. The contribution of higher modes was found to be less than 15% relative to the first bending modes. The relationship between the square of mean wind speed and the alongwind and crosswind displacement was studied and they were found to be highly correlated. In addition, the standard deviation of wind speed fluctuations and response fluctuations were found to be partially correlated.

Because of the structural simplicity, availability of the structural properties, and availability of simultaneous measurement of wind-and-structural response time history for the two downburst case studies, this research will serve as one of the stepping stones toward validation of analytical downburst wind load calculation techniques. Validation of selected analytical downburst wind load calculation methods will be presented in future publications. However, to extend the validation to the common structures susceptible to downburst-induced damages, similar full-scale wind-and-structural response monitoring are necessary for various groups of structures. Future monitoring stations might have to consider the installation of additional meteorological measurements such as temperature, atmospheric pressure, and relative humidity sensors on the monitored structures to facilitate the separation of downburst events from other gust fronts and ABL winds. Although wind speed was registered only at the top of the monitored structure, the installation of anemometers at various heights of monitored structures is highly recommended for future studies, to validate the existing vertical profile of the mean wind speed and turbulent wind field models.

CRediT authorship contribution statement

Mekdes T. Mengistu: Conceptualization, Methodology, Validation, Investigation, Visualization, Writing – original draft. **Andrea Orlando:** Investigation, Data curation, Writing – review & editing. **Maria Pia Repetto:** Conceptualization, Methodology, Resources, Writing – review & editing, Funding acquisition.

Declaration of competing interest

The authors declare that they have no known competing financial interests or personal relationships that could have appeared to influence the work reported in this paper.

Data availability

The data that has been used is confidential.

Acknowledgments

The contribution of the third author is funded by the European Research Council (ERC) under the European Union's Horizon 2020 research and innovation program (grant agreement No. 741273) for the project "THUNDERR - Detection, simulation, modeling and loading of thunderstorm outflows to design wind-safer and cost-efficient structures" – through an Advanced Grant 2016. The monitoring system is co-funded by the Italian Ministry of Instruction and Scientific Research (MIUR), Prot. 2015TTJN95 in the framework of the Research Project of Relevant National Interest (PRIN 2015).

References

Aboshosha, H., Bitsuamlak, G., El Damatty, A., 2015. Turbulence characterization of downbursts using LES. J. Wind Eng. Ind. Aerodyn. (ISSN: 01676105) 136, 44–61. http://dx.doi.org/10.1016/j.jweia.2014.10.020.

Asano, K., Iida, Y., Uematsu, Y., 2019. Laboratory study of wind loads on a low-rise building in a downburst using a moving pulsed jet simulator and their comparison with other types of simulators. J. Wind Eng. Ind. Aerodyn. (ISSN: 0167-6105) 184, 313–320. http://dx.doi.org/10.1016/J.JWEIA.2018.11.034.

Brincker, R., Ventura, C.E., Andersen, P., 2001. Damping estimation by frequency domain decomposition. In: Proc. IMAC 19. pp. 698–703.

Brincker, R., Zhang, L., 2009. Frequency domain decomposition revisited. In: Proc. 3rd Int. Oper. Modal Anal. Conf., vol. 2. ISBN: 5555555555, pp. 615–626.

Brusco, S., Lerzo, V., Solari, G., 2019. Directional response of structures to thunderstorm outflows. Meccanica (ISSN: 15729648) 54, 1281–1306. http://dx.doi.org/10.1007/s11012-019-00986-5,

Burlando, M., Zhang, S., Solari, G., 2018. Monitoring, cataloguing, and weather scenarios of thunderstorm outflows in the northern Mediterranean. Nat. Hazards Earth Syst. Sci. (ISSN: 16849981) 18, 2309–2330. http://dx.doi.org/10.5194/nhess-18-2309-2018.

Carassale, L., Percivale, F., 2008. Modal identification of wind-Excited slender structures by acceleration and strain measurements. In: 7th Eur. Conf. Struct. Dyn. EURODYN 2008. Southampton, ISBN: 9780854328826.

Chay, M.T., Albermani, F., Wilson, R., 2006. Numerical and analytical simulation of downburst wind loads. Eng. Struct. (ISSN: 01410296) 28, 240–254. http://dx.doi.org/10.1016/j.engstruct.2005.07.007.

Chay, M.T., Letchford, C.W., 2002. Pressure distributions on a cube in a simulated thunderstorm downburst—Part A: stationary downburst observations. J. Wind Eng. Ind. Aerodyn. (ISSN: 0167-6105) 90, 711–732. http://dx.doi.org/10.1016/S0167-6105(02)00158-7.

Chen, X., 2008. Analysis of alongwind tall building response to transient nonstationary winds. J. Struct. Eng. (ISSN: 0733-9445) 134, 782–791. http://dx.doi.org/10.1061/(ASCE)0733-9445(2008)134:5(782).

Chen, L., Letchford, C.W., 2004. A deterministic-stochastic hybrid model of downbursts and its impact on a cantilevered structure. Eng. Struct. (ISSN: 01410296) 26, 619–629. http://dx.doi.org/10.1016/j.engstruct.2003.12.009.

Choi, E.C., Hidayat, F.A., 2002. Gust factors for thunderstorm and non-thunderstorm winds. J. Wind Eng. Ind. Aerodyn. (ISSN: 01676105) 90, 1683–1696. http://dx.doi.org/10.1016/S0167-6105(02)00279-9.

Choi, E.C., Tanurdjaja, A., 2002. Extreme wind studies in Singapore. An area with mixed weather system. J. Wind Eng. Ind. Aerodyn. (ISSN: 01676105) 90, 1611–1630. http://dx.doi.org/10.1016/S0167-6105(02)00274-X.

Cole, H.A., 1973. On-line failure detection and damping measurement of aerospace structures by random decrement signatures. In: NASA Contract. Reports. (ISSN: 05657059) ISBN: 1973001020.

Cook, N.J., Ian Harris, R., Whiting, R., 2003. Extreme wind speeds in mixed climates revisited. J. Wind Eng. Ind. Aerodyn. (ISSN: 01676105) 91, 403–422. http://dx.doi.org/10.1016/S0167-6105(02)00397-5.

De Gaetano, P., Repetto, M.P., Repetto, T., Solari, G., 2014. Separation and classification of extreme wind events from anemometric records. J. Wind Eng. Ind. Aerodyn. (ISSN: 01676105) 126, 132–143. http://dx.doi.org/10.1016/j.jweia.2014.01.006.

Durañona, V., Sterling, M., Baker, C.J., 2007. An analysis of extreme non-synoptic winds. J. Wind Eng. Ind. Aerodyn. (ISSN: 01676105) 95, 1007–1027. http://dx.doi.org/10.1016/j.jweia.2007.01.014.

Eng. Sci. Data Unit, D.I., 1985. ESDU 84030.

Fujita, T., 1985. The downburst-micoburst and macroburst report of projects NIMROD and JAWS. In: Rep. Proj. NIMROD JAWS. p. 128.

Holmes, J., Forristall, G., Mcconochie, J., 2005. Dynamic response of structures to thunderstorm winds. In: 10th Am. Conf. Wind Eng. ACWE 2005. (ISSN: 1365-0556) http://dx.doi.org/10.1002/pse.132.

Huang, G., Jiang, Y., Peng, L., Solari, G., Liao, H., Li, M., 2019. Characteristics of intense winds in mountain area based on field measurement: Focusing on thunderstorm winds. J. Wind Eng. Ind. Aerodyn. (ISSN: 01676105) 190, 166–182. http://dx.doi.org/10.1016/j.jweia.2019.04.020.

Iida, Y., Uematsu, Y., 2019. Numerical study of wind loads on buildings induced by downbursts. J. Wind Eng. Ind. Aerodyn. (ISSN: 0167-6105) 191, 103–116. http://dx.doi.org/10.1016/J.JWEIA.2019.05.018.

Jesson, M., Sterling, M., Letchford, C., Baker, C., 2015a. Aerodynamic forces on the roofs of low-, mid- and high-rise buildings subject to transient winds. J. Wind Eng. Ind. Aerodyn. (ISSN: 01676105) 143, 42–49. http://dx.doi.org/10.1016/J.JWEIA.2015.04.020.

Jesson, M., Sterling, M., Letchford, C., Haines, M., 2015b. Aerodynamic forces on generic buildings subject to transient, downburst-type winds. J. Wind Eng. Ind. Aerodyn. (ISSN: 0167-6105) 137, 58–68. http://dx.doi.org/10.1016/J.JWEIA.2014.12.003.

Junayed, C., Jubayer, C., Parvu, D., Romanic, D., Hangan, H., 2019. Flow field dynamics of large-scale experimentally produced downburst flows. J. Wind Eng. Ind. Aerodyn. (ISSN: 01676105) 188, 61–79. http://dx.doi.org/10.1016/j.jweia.2019.02.008.

Kim, J., Hangan, H., 2007. Numerical simulations of impinging jets with application to downbursts. J. Wind Eng. Ind. Aerodyn. (ISSN: 01676105) 95, 279–298. http://dx.doi.org/10.1016/j.jweia.2006.07.002.

Kwon, D.K., Kareem, A., 2009. Gust-front factor: New framework for wind load effects on structures. J. Struct. Eng. (ISSN: 07339445) 135, 717–732. http://dx.doi.org/10.1061/(ASCE)0733-9445(2009)135:6(717).

Le, V., Caracoglia, L., 2019. Generation and characterization of a non-stationary flow field in a small-scale wind tunnel using a multi-blade flow device. J. Wind Eng. Ind. Aerodyn. (ISSN: 01676105) 186, 1–16. http://dx.doi.org/10.1016/j.jweia.2018.12.017.

Letchford, C.W., Mans, C., Chay, M.T., 2002. Thunderstorms - Their importance in wind engineering (a case for the next generation wind tunnel). J. Wind Eng. Ind. Aerodyn. (ISSN: 01676105) 90, 1415–1433. http://dx.doi.org/10.1016/S0167-6105(02)00262-3.

Lombardo, F.T., Main, J.A.M., Simiu, E., 2009. Automated extraction and classification of thunderstorm and non-thunderstorm wind data for extreme-value analysis. J. Wind Eng. Ind. Aerodyn. (ISSN: 01676105) 97, 120–131. http://dx.doi.org/10.1016/j.jweia.2009.03.001.

Lombardo, F.T., Mason, M.S., de Alba, A.Z., 2018. Investigation of a downburst loading event on a full-scale low-rise building. J. Wind Eng. Ind. Aerodyn. (ISSN: 0167-6105) 182, 272–285. http://dx.doi.org/10.1016/J.JWEIA.2018.09.020.

Mason, M.S., Letchford, C.W., James, D.L., 2005. Pulsed wall jet simulation of a stationary thunderstorm downburst, Part A: Physical structure and flow field characterization. J. Wind Eng. Ind. Aerodyn. (ISSN: 01676105) 93, 557–580. http://dx.doi.org/10.1016/j.jweia.2005.05.006.

McConville, A., Sterling, M., Baker, C., 2009. The physical simulation of thunderstorm downbursts using an impinging jet. Wind Struct. 12, 133–149.

Orlando, A., 2021. Full-scale Monitoring of the Wind-Induced Response of Vertical Slender Structures , with Fixed and Rotating Masses (Ph.D. thesis). University of Genoa.

Orlando, A., Pagnini, L., Pia Repetto, M., 2023. Wind tunnel tests of a hexadecagonal cylinder with imperfections and ancillaries: aerodynamic characterization and technical discussion. Eng. Struct. (ISSN: 18737323) 274, 115114. http://dx.doi.org/10.1016/j.engstruct.2022.115114.

Pagnini, L., Piccardo, G., Repetto, M.P., 2018. Full scale behavior of a small size vertical axis wind turbine. Renew. Energy (ISSN: 18790682) 127, 41–55. http://dx.doi.org/10.1016/j.renene.2018.04.032.

Piccardo, G., Solari, G., 2000. 3D wind-excited response of slender structures: closed-form solution. ASCE 936–943. http://dx.doi.org/10.1061/(asce)0733-9445(2000)126:8(936).

Repetto, M.P., Burlando, M., Solari, G., De Gaetano, P., Pizzo, M., 2017. Integrated tools for improving the resilience of seaports under extreme wind events. Sustain. Cities Soc. (ISSN: 22106707) 32, 277–294. http://dx.doi.org/10.1016/j.scs.2017.03.022.

Romanic, D., LoTufo, J., Hangan, H., 2019. Transient behavior in impinging jets in crossflow with application to downburst flows. J. Wind Eng. Ind. Aerodyn. (ISSN: 01676105) 184, 209–227. http://dx.doi.org/10.1016/j.jweia.2018.11.020.

Roncallo, L., Solari, G., 2020. An evolutionary power spectral density model of thunderstorm outflows consistent with real-scale time-history records. J. Wind Eng. Ind. Aerodyn. (ISSN: 01676105) 203, 104204. http://dx.doi.org/10.1016/j.jweia.2020.104204.

Sengupta, A., Haan, F.L., Sarkar, P.P., Balaramudu, V., 2008. Transient loads on buildings in microburst and tornado winds. J. Wind Eng. Ind. Aerodyn. (ISSN: 01676105) 96, 2173–2187. http://dx.doi.org/10.1016/j.jweia.2008.02.050.

Solari, G., 1993. Gust buffeting. I: Peak wind velocity and equivalent pressure. J. Struct. Eng. 119, 365–382.

Solari, G., 2016. Thunderstorm response spectrum technique: Theory and applications. Eng. Struct. (ISSN: 01410296) 108, 28–46. http://dx.doi.org/10.1016/j.engstruct.2015.11.012.

Solari, G., 2020. Education and dissemination in wind science and engineering. J. Wind Eng. Ind. Aerodyn. (ISSN: 01676105) 203, 104241. http://dx.doi.org/10.1016/j.jweia.2020.104241.

Solari, G., Burlando, M., De Gaetano, P., Repetto, M.P., 2015a. Characteristics of thunderstorms relevant to the wind loading of structures. Wind Struct. An Int. J. (ISSN: 12266116) 20, 763–791. http://dx.doi.org/10.12989/was.2015.20.6.763.

Solari, G., Burlando, M., Repetto, M.P., 2020. Detection, simulation, modelling and loading of thunderstorm outflows to design wind-safer and cost-efficient structures. J. Wind Eng. Ind. Aerodyn. (ISSN: 01676105) 200, 104142. http://dx.doi.org/10.1016/j.jweia.2020.104142.

Solari, G., De Gaetano, P., Repetto, M.P., 2015b. Thunderstorm response spectrum: Fundamentals and case study. J. Wind Eng. Ind. Aerodyn. 143, 62–77. http://dx.doi.org/10.1016/j.jweia.2015.04.009.

Solari, G., Rainisio, D., De Gaetano, P., 2017. Hybrid simulation of thunderstorm outflows and wind-excited response of structures. Meccanica (ISSN: 15729648) 52, 3197–3220. http://dx.doi.org/10.1007/s11012-017-0718-x.

Stengel, D., Thiele, K., 2017. Measurements of downburst wind loading acting on an overhead transmission line in Northern Germany. Procedia Eng. (ISSN: 18777058) 199, 3152–3157. http://dx.doi.org/10.1016/j.proeng.2017.09.578.

Tamura, Y., Zhang, L., Yoshida, A., Nakata, S., Itoh, T., 2002. Ambient vibration tests and modal identification of structures by FDD and 2DOF-RD technique. In: Proc. Struct. Eng. World Congr.. Yokohama, Japan.

Twisdale, L.A., Vickery, P.J., 1992. Research on thunderstorm wind design parameters. J. Wind Eng. Ind. Aerodyn. (ISSN: 01676105) 41, 545–556. http://dx.doi.org/10.1016/0167-6105(92)90461-I.

Vermeire, B.C., Orf, L.G., Savory, E., 2011. Improved modelling of downburst outflows for wind engineering applications using a cooling source approach. J. Wind Eng. Ind. Aerodyn. (ISSN: 01676105) 99, 801–814. http://dx.doi.org/10.1016/j.jweia.2011.03.003.

Welch, P.D., 1967. The use of fast Fourier transform for the estimation of power spectra: A method based on time averaging over short, modified periodograms. IEEE Trans. Audio Electroacoust. (ISSN: 00189278) 15, 70–73. http://dx.doi.org/10.1109/TAU.1967.1161901.

Wu, Z., Iida, Y., Uematsu, Y., 2021. The flow fields generated by stationary and travelling downbursts and resultant wind load effects on transmission line structural system. J. Wind Eng. Ind. Aerodyn. (ISSN: 0167-6105) 210, 104521. http://dx.doi.org/10.1016/J.JWEIA.2021.104521.

Zhang, L., Brincker, R., Andersen, P., 2005. An overview of operational modal analysis. In: Proc. 1st Int. Oper. Modal Anal. Conf.. pp. 179–190.

Zhang, S., Solari, G., Burlando, M., Yang, Q., 2019. Directional decomposition and properties of thunderstorm outflows. J. Wind Eng. Ind. Aerodyn. (ISSN: 01676105) 189, 71–90. http://dx.doi.org/10.1016/j.jweia.2019.03.014.

Zhang, H., Wang, H., Xu, Z., Zhang, Y., Tao, T., Mao, J., 2022. Monitoring-based analysis of wind-induced vibrations of ultra-long stay cables during an exceptional wind event. J. Wind Eng. Ind. Aerodyn. (ISSN: 01676105) 221, 104883. http://dx.doi.org/10.1016/j.jweia.2021.104883.